

# Untangling the Mechanisms of Lattice Distortions in Biogenic Crystals across Scales

Vanessa Schoeppler, Phil K. Cook, Carsten Detlefs, Raffaella Demichelis, and Igor Zlotnikov\*

**Biomaterialized structures are complex functional hierarchical assemblies composed of biomineral building blocks joined together by an organic phase. The formation of individual mineral units is governed by the cellular tissue component that orchestrates the process of biomineral nucleation, growth, and morphogenesis. These processes are imprinted in the structural, compositional, and crystallographic properties of the emerging biominerals on all scales. Measurement of these properties can provide crucial information on the mechanisms that are employed by the organism to form these complex 3D architectures and to unravel principles of their functionality. Nevertheless, so far, this has only been possible at the macroscopic scale, by averaging the properties of the entire composite assembly, or at the mesoscale, by looking at extremely small parts of the entire picture. In this study, the newly developed synchrotron-based dark-field X-ray microscopy method is employed to study the link between 3D crystallographic properties of relatively large calcitic prisms in the shell of the mollusc *Pinna nobilis* and their local lattice properties with extremely high angular resolution down to 0.001°. Mechanistic links between variations in local lattice parameters and spacing, crystal orientation, chemical composition, and the deposition process of the entire mineral unit are unraveled.**

## 1. Introduction

Minerals formed by living organisms are significantly different from their synthetic and geological analogs.<sup>[1]</sup> Being a building block of a larger hierarchically structured composite material system, biominerals play an important role in the performance of the entire structure.<sup>[2]</sup> Since they are inherently stiffer and harder than most of the organic components, in many cases, biominerals provide the animals with mechanically related functionality. Some common examples are protection against predation in the case of molluscan shells,<sup>[3]</sup> structural support in the case of vertebrate endoskeletons,<sup>[4]</sup> or crushing/grinding in the case of teeth.<sup>[5]</sup> However, magnetic and optical functionalities, such as magnetotaxis implemented by magnetotactic bacteria<sup>[6]</sup> and light manipulation in the cystoliths of some plants,<sup>[7]</sup> are also observed. In all these examples, the characteristics of the mineral units, on all scales, from crystal lattice properties

on the atomic scale to the shape of the entire unit on the macroscopic scale, reflect hundreds of millions of years of evolution through functional adaptation and enable the organisms to perform a specific task. Therefore, the process of biomineralization is strictly controlled by the cellular components that orchestrate the process of biomineral nucleation, growth, and morphogenesis.


For almost two centuries, numerous studies have been attempted to understand the biochemistry and the physics behind biominerals formation, properties, and function. As it is in most cases not possible to observe the process of biomineralization in vivo, this research is usually focused on characterizing the final or a transient stage of growth ex vivo. The entire history of biogenic mineral formation is embedded in its structure and is reflected in its properties. Therefore, detailed compositional, structural, and crystallographic analysis of the mineral building blocks can provide ample information on how they were grown or, in other words, on the mechanisms that were employed by the living tissue to guide the emergence of the mineral phase.<sup>[8–12]</sup> Although state-of-the-art materials characterization techniques and biochemical methods were employed to generate abundant knowledge on various biomineralization processes, until now, a detailed across-scale correlative study of biogenic

V. Schoeppler, I. Zlotnikov  
B CUBE – Center for Molecular Bioengineering  
Technische Universität Dresden  
01069 Dresden, Germany  
E-mail: igor.zlotnikov@tu-dresden.de

V. Schoeppler  
Department of Physics  
University of California  
Berkeley, CA 94720, USA

P. K. Cook, C. Detlefs  
ESRF – The European Synchrotron  
Grenoble 38000, France

R. Demichelis  
Curtin Institute for Computation  
The Institute for Geoscience Research (TIGeR)  
School of Molecular and Life Sciences  
Curtin University  
Perth, Western Australia 6845, Australia

 The ORCID identification number(s) for the author(s) of this article can be found under <https://doi.org/10.1002/adma.202200690>.

© 2022 The Authors. Advanced Materials published by Wiley-VCH GmbH. This is an open access article under the terms of the Creative Commons Attribution-NonCommercial License, which permits use, distribution and reproduction in any medium, provided the original work is properly cited and is not used for commercial purposes.

DOI: 10.1002/adma.202200690

minerals was never achieved. For example, the measurement of lattice parameters was only possible using X-ray scattering methods on the macroscopic scale, averaging the local crystallographic properties of the studied composite assemblies;<sup>[13,14]</sup> or on the mesoscale, by looking at extremely small crop-outs of the entire picture.<sup>[15,16]</sup> The same can be said about crystal orientation and the mosaicity and crystallographic coherence of single biomineral units. Here, electron backscatter diffraction (EBSD) is an extremely powerful tool to study the texture of mineralized tissues. EBSD is, however, limited to 2D and a relatively low angular resolution.<sup>[17]</sup> Finally, the shape of the mineral units in 3D is commonly visualized using various electron microscopy-based and X-ray-based tomography methods.<sup>[18–20]</sup> These approaches require delicate instrumentation and cannot be performed simultaneously on the same sample. Hence, local crystallographic properties of biomineral units, such as lattice distortions and misorientations and, most importantly, their link to the shape of the entire unit were never previously uncovered. In this regard, the new dark-field X-ray microscopy (DFXM) method, recently developed at the beamline ID06-HXM of the European Synchrotron in Grenoble, France (ESRF), provides a unique opportunity to study the crystallographic properties of relatively large (hundreds of micrometers in size) crystalline units while providing information on local lattice properties (on the sub-micrometer scale) with extremely high angular resolution down to  $0.001^\circ$ .<sup>[21,22]</sup>

## 2. Results and Discussion

Out of over 60 biologically formed minerals, calcium carbonate ( $\text{CaCO}_3$ ) is the most abundant in nature, found in a large variety of the most complex shapes and structures.<sup>[1]</sup> The chemistry and physics of  $\text{CaCO}_3$  nucleation and growth is also one of the most studied topics in biomineralization and other related disciplines. Nevertheless, biological morphogenesis of calcium carbonate is poorly understood. Multiple studies suggest that the intra-crystalline macromolecular organic matter (sugars and proteins) and substitutional lattice impurities ( $\text{Mg}^{2+}$  and  $\text{Sr}^{2+}$  instead of  $\text{Ca}^{2+}$ ) are used by the organisms to control the thermodynamics and the kinetics of the crystallization process and, hence, morph the mineral phase.<sup>[23–29]</sup> Furthermore, recent findings demonstrate that lattice distortions and mosaicity, which reflect the presence of the described impurities and indicate the occurrence of residual stresses in biominerals not only play a significant role in their mechanical performance but also carry crucial information on their growth process.<sup>[30–34]</sup>

Molluscan shells exhibit a species-specific sequence of shell ultrastructures, each assembled from individual mineral building blocks made of calcium carbonate (calcite or aragonite) joined together by an organic phase.<sup>[9,35,36]</sup> While each ultrastructure has its unique architecture, they are all formed extracellularly in an extrapallial space, where the shell grows unidirectionally in thickness, between its outer organic skin (periostracum) and the epithelial cells layer of the mantle. Specifically, the shell of *P. nobilis* (Figure 1a) is composed of two extensively studied

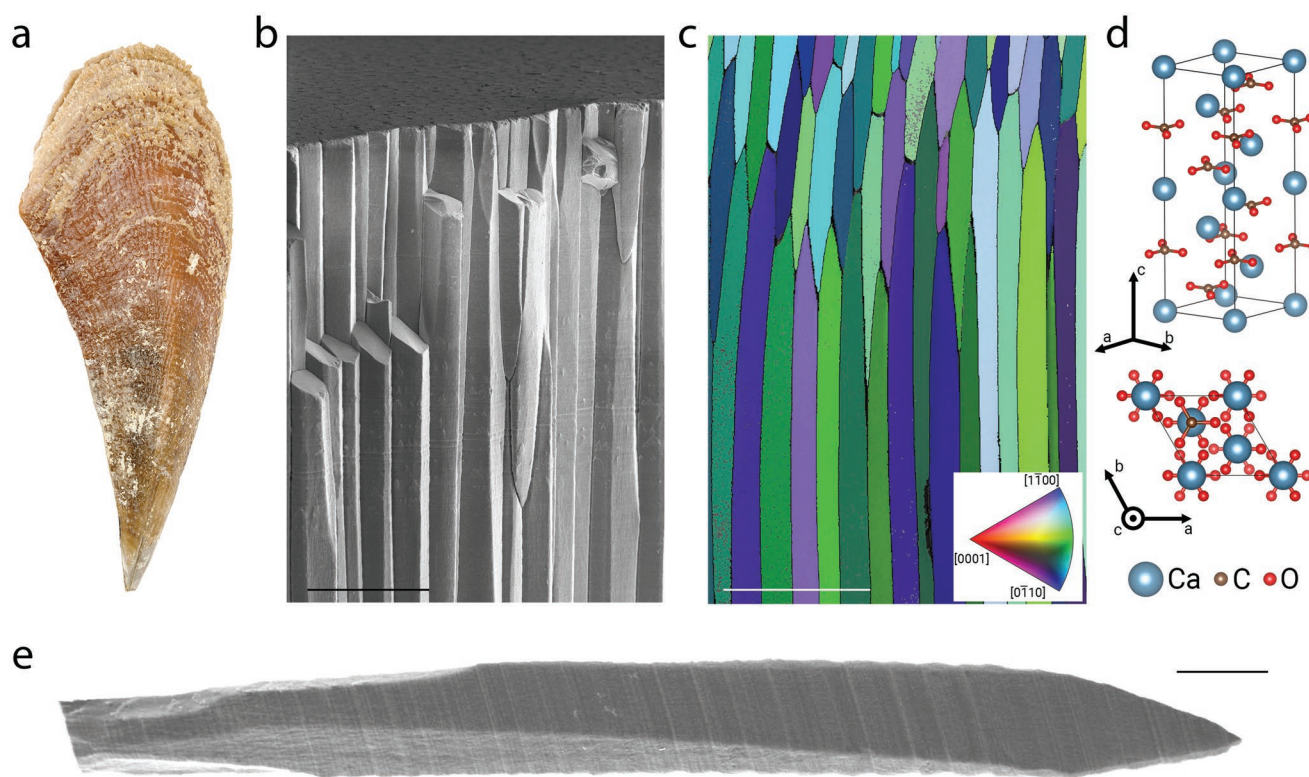


**Figure 1.** Morphology and crystal orientation of the prismatic ultrastructure in *Pinna nobilis*. a) The bivalve shell of *P. nobilis*. b) SEM image of a fractured cross-section of the prismatic architecture in *P. nobilis* imaged perpendicular to the direction of growth. Scale bar: 100  $\mu\text{m}$ . c) Electron backscatter diffraction (EBSD) map of the prismatic layer oriented perpendicular to the direction of growth. Scale bar: 200  $\mu\text{m}$ . Insert: the corresponding color-coded inverse pole figure of calcite, with the reference direction normal to the image plane. d) A ball and stick representation of the crystallographic structure of calcite. e) Scanning electron microscopy image of an individual calcitic prism isolated from the shell. Scale bar: 50  $\mu\text{m}$ . Periodic growth bands are clearly visible.

ultrastructures—nacreous and prismatic.<sup>[8]</sup> Nacre appears as a thin layer on the inner surface of the shell and consists of a few hundreds of nanometers thick polygonal aragonite tablets made of aragonite stacked to form a highly periodic layered ultrastructure. The prismatic layer makes up the main portion of the shell and is composed of comparatively large calcitic columnar units (prisms) that are several tens of micrometers wide and can reach a length of a few millimeters (Figure 1b,c).

The prisms in *P. nobilis* were classically described as perfect single crystalline entities.<sup>[37–43]</sup> This postulation is based on observations made by methods such as polarized light microscopy,<sup>[29]</sup> X-ray diffraction and EBSD,<sup>[42]</sup> which are techniques that are widely used to study molluscan shells. Whereas these methods have the advantage of allowing a relatively fast analysis of large samples composed of various minerals and large misorientation angles, they are limited in spatial and angular resolution. For example, an EBSD map of a longitudinal cross-section of the prismatic layer in *P. nobilis* (Figure 1c) suggests that the individual prisms are perfect single crystals with the *c*-axis of calcite (Figure 1d) being almost parallel to the long-axes of the prisms, typical for *P. nobilis* prisms.<sup>[44]</sup> Here, calcite is described by a hexagonal unit cell (Figure 1d). More recently,

however, nanoscale mosaicity and local lattice distortions of calcite prisms in *P. nobilis* and other mollusks was revealed by a number of novel X-ray-based methods.<sup>[15,16]</sup> These studies, once again, demonstrate that, indeed, biominerals are intricate inhomogeneous entities the properties and the shape of which are regulated on all scales: from the effects of inorganic substitutional impurities and mineral lattice interaction with organic interstitial macromolecules on the atomistic scale to macroscopic driving forces, such as environmental and geometric boundary conditions.<sup>[10,12]</sup>

To study lattice distortions in biogenic calcite, individual prisms from the shell of *P. nobilis* (Figure 1e) were investigated using DFXM. First, retractable near-field detectors were used to image the sample, identify a suitable diffraction plane, and obtain spatial information in full field conditions (Figure 2a). Since the calcitic {10 $\bar{1}$ 4} lattice plane family provides the most intense diffraction signal, this specific Bragg reflection was used for orientation and lattice spacing mapping with DFXM (Figure 2b). To fulfill the Bragg condition, the sample was mounted with the prism's long-axis, which is almost parallel to the calcitic *c*-axis, laying in the *x*-*z* plane of the laboratory coordinate system and tilted by  $\approx 45^\circ$  around the *y*-axis (Figure 2a).

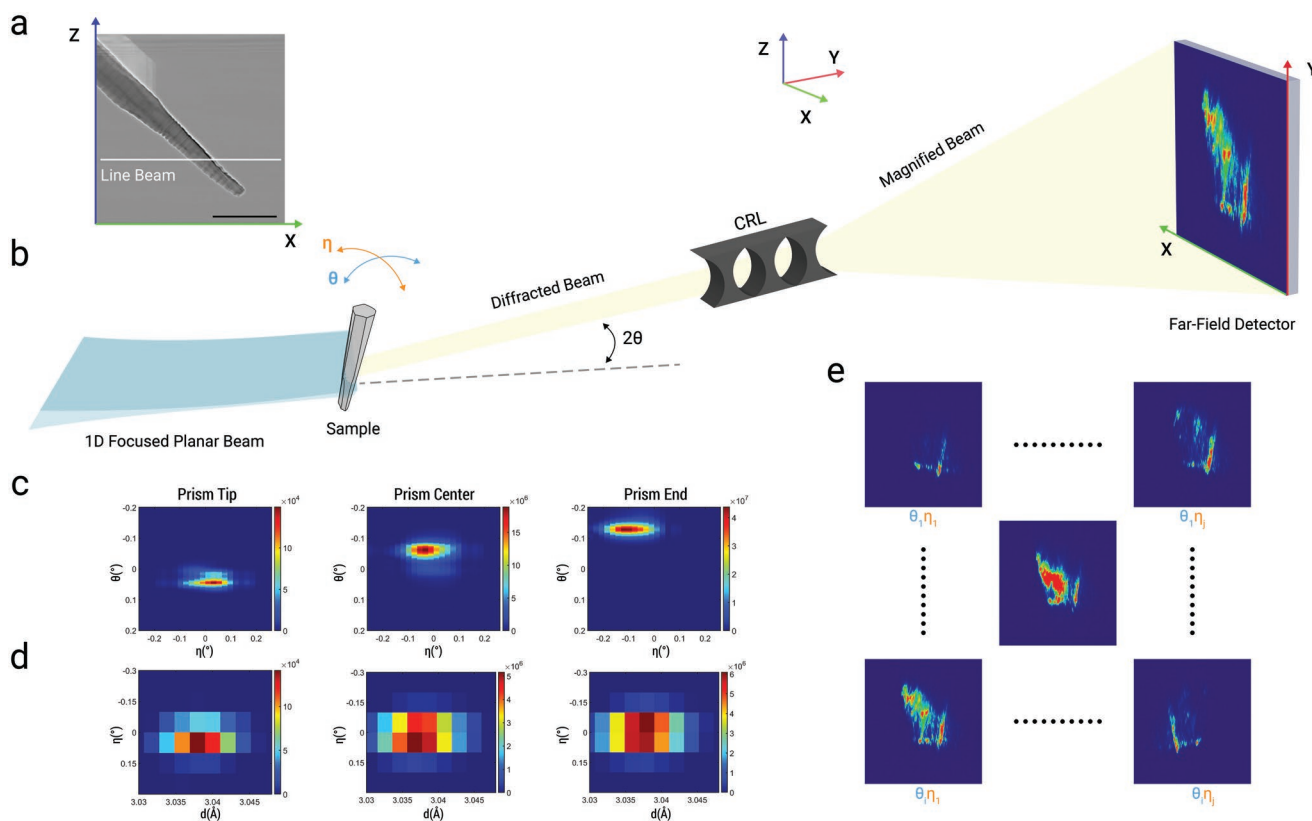


**Figure 2.** Experimental DFXM setup for the analysis of an isolated *P. nobilis* prism. a) Radiograph of the mounted *P. nobilis* prism. The prism long-axis is tilted  $45^\circ$  around the laboratory *y*-axis to fit the Bragg conditions ( $2\theta$ ) for the calcitic  $\{10\bar{1}4\}$  plane. Scale bar:  $100\ \mu\text{m}$ . b) DFXM setup: a series of orientation and strain maps of the prism where acquired by illuminating the sample with a condensed monochromatic line beam (i.e.,  $400\ \mu\text{m} \times 200\ \text{nm}$ ) and stepwise ( $1\ \mu\text{m}$ ) moving the sample along the lab *z*-axis. At every step, the diffracted signal from the calcitic  $\{10\bar{1}4\}$  plane is magnified by a set of CRLs that project the real-space images of the sample onto the far-field detector. The orientation of the scattering vector  $G_{104}$  is varied by tilting the sample in the two perpendicular directions  $\theta$  and  $\eta$  while acquiring images. Variations in lattice spacing where determined by scanning through the Bragg angle  $2\theta$  by moving the optics and by tilting the sample in the  $\eta$  direction. c,d) Summed intensity maps of the  $\theta$  and  $\eta$  tilt (c) and the *d*-spacing (d) measurements for individual scans acquired at the tip, the center, and the end of the *z*-scan range, from left to right, respectively. e) A Gaussian moment fit is used to identify the maximum intensity for each pixel at every step.



As the sample is illuminated with a 1D focused planar beam in the  $x$ - $y$  plane,<sup>[45]</sup> this experimental set-up allows for a 3D imaging of the prism using a series of oblique cross-sections taken in the  $z$ -direction.

During measurement, the projection on the detector is a real-space image resembling an  $x$ - $y$  slice through the prism generated by magnifying compound refractive lenses (CRLs) (Figure 2b). Orientation maps were acquired by collecting a series of images while tilting the sample on two axes  $\eta$  and  $\theta$ . Maps of  $d$ -spacing were obtained by scanning through five positions of the Bragg angle  $2\theta$ .<sup>[21,22]</sup> 3D maps of the prisms were generated by moving the sample vertically in the  $z$ -direction using 1  $\mu\text{m}$  steps along the first 100  $\mu\text{m}$  of the prism for the orientation mapping and the first 25  $\mu\text{m}$  for lattice spacing mapping. In this work, as a consequence of vertical motion, tilting increments and X-ray optics, a pixel size of 78 and 315 nm in  $x$ , and  $y$  directions, respectively, and an angular resolution of  $0.01^\circ$  were achieved. Summed intensity maps corresponding to slices taken from the beginning, center and end of the scan range for orientation (Figure 2c) and lattice spacing (Figure 2d) mapping confirm the integrity of both datasets. Here, the orientation

and  $d$ -spacing are determined by following the changes in pixel intensities in every image of the tilt series. In each slice, the local lattice properties are determined by identifying the angles  $\eta$  and  $\theta$  that provide the maximum intensity at every pixel. This way, real space images of the mosaicity and lattice distortions of the illuminated cross-sections of the prism can be generated.

Representative 2D slices through the prism depict the ability of DFXM to provide detailed information on the local crystallographic orientation (Figure 3a) and lattice spacing (Figure 3b) of biogenic calcite in the prisms of *P. nobilis*. Indeed, these data provide a picture that is significantly different from that obtained using EBSD (Figure 1c). In agreement with recent reports on local mosaicity and averaged lattice distortions, these maps show intricate patterns of lattice incoherence and distortion. However, most importantly, these data allow us to correlate between these two local effects on the scale of the entire prism.

Both maps, Figure 3a,b, demonstrate a distinct striation pattern where the lattice rotates back and forth by approximately a tenth of a degree, and the  $d$ -spacing,  $d$ , between the  $\{10\bar{1}4\}$  lattice planes alternates between 3.028  $\text{\AA}$  and an increased value of 3.041  $\text{\AA}$ .

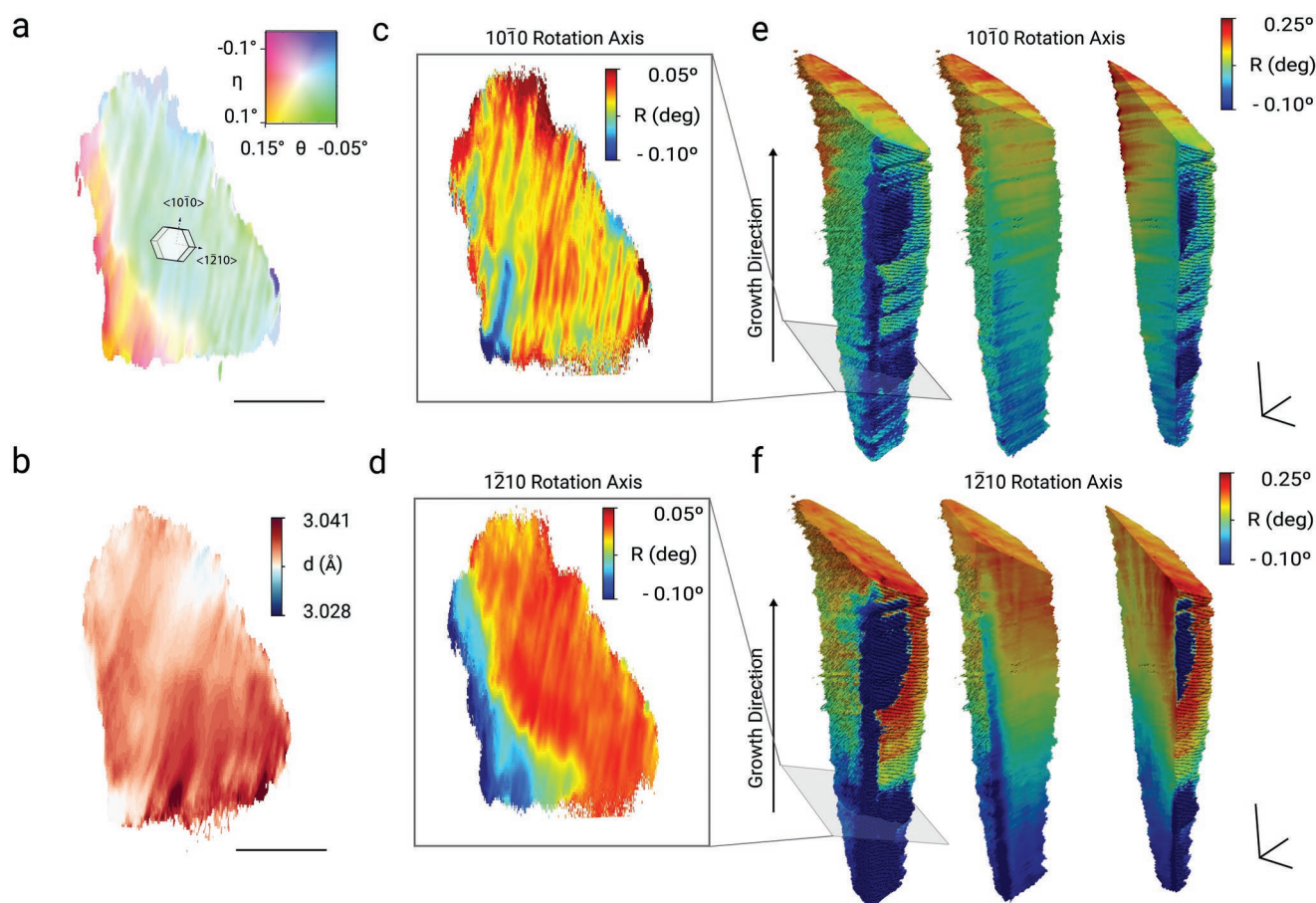


**Figure 3.** 2D and 3D analysis of lattice distortions within a *P. nobilis* prism. a,b) Mosaicity and  $d$ -spacing maps of the calcitic  $\{10\bar{1}4\}$  plane of a representative slice taken from the 3D stack obtained by DFXM, respectively. Scale bars: 10  $\mu\text{m}$ . c,d) Relative lattice rotation around the  $[10\bar{1}0]$  and  $[\bar{1}2\bar{1}0]$  axes, respectively, calculated as the change in an angle between the local calcitic  $c$ -axis and the mean crystal direction  $[1\bar{2}10]$  and  $[10\bar{1}0]$  that are indicated in (a), respectively. e,f) 3D reconstructions of the lattice rotation around the  $[10\bar{1}0]$  axis (e) and the  $[\bar{1}2\bar{1}0]$  axis (f) showing the entire volume of the first 100  $\mu\text{m}$  of the prism and two perpendicular longitudinal sections from left to right, respectively. Isometric scale bars are 20  $\mu\text{m}$ .

These data can be compared to crystallographic information averaged over the entire prismatic ultrastructure in *P. nobilis* measured using high resolution powder diffraction by Pokroy et al.<sup>[13]</sup> Here, the mean spacing between the  $\{10\bar{1}4\}$  lattice planes was shown to be 3.0328 Å calculated with lattice parameters  $a = 4.98138$  Å and  $c = 1705803$  Å. This  $d$ -space value falls between the two extreme values obtained in this study using DFXM.

Using the full-field diffraction analysis performed prior to DFXM measurements, the real orientation of calcite inside the prism was calculated (Figure 3a). The observed striations follow specific crystal directions that run parallel to the  $[10\bar{1}0]$  direction of calcite. The local degree of rotation around the  $[10\bar{1}0]$ -axis and around its perpendicular, the  $[1\bar{2}10]$ -axis, were calculated by measuring the change in the angle between the local direction of the  $c$ -axis of calcite at each pixel and fixed mean directions of  $[1\bar{2}10]$  and  $[10\bar{1}0]$ , respectively, averaged over the entire data set, Figure 3c,d, respectively. These maps confirm that the observed striations are the result of lattice rotation around the  $[10\bar{1}0]$ -axis of calcite, whereas the rotation around the  $[1\bar{2}10]$ -axis reveals a gradual twist of the lattice throughout the entire prism.

Similar analysis was performed to characterize all 2D slices through the prisms, which, when stitched together, provide an unprecedented view on local lattice properties of biogenic calcite in 3D. Longitudinal and transverse sections of lattice rotation data around the  $[10\bar{1}0]$ -axis (Figure 3e) demonstrate that the observed striations are continuous layers that run perpendicular to the long-axis of the prism. The width of the bands is irregular and varies from 5 to 15  $\mu\text{m}$  but appear consistent throughout the entire length of the prism. Furthermore, the average orientation changes gradually along the growth direction over the measured range of 100  $\mu\text{m}$  by  $0.35^\circ$ . This lattice twist is more distinct when observing the rotation around the  $[1\bar{2}10]$ -axis where the horizontal bands are hardly visible (Figure 3f).

Finally, the 3D reconstruction of the  $d$ -spacing between  $(10\bar{1}4)$  lattice planes of the first 25  $\mu\text{m}$  was compared to the lattice rotation behavior. In order to link changes in lattice spacing and orientation along the prism's long-axis, values averaged over lines drawn perpendicular to the direction of growth for every longitudinal slice through the prisms were calculated for all three datasets:  $d$ -spacing between  $(10\bar{1}4)$  planes (Figure 4a),

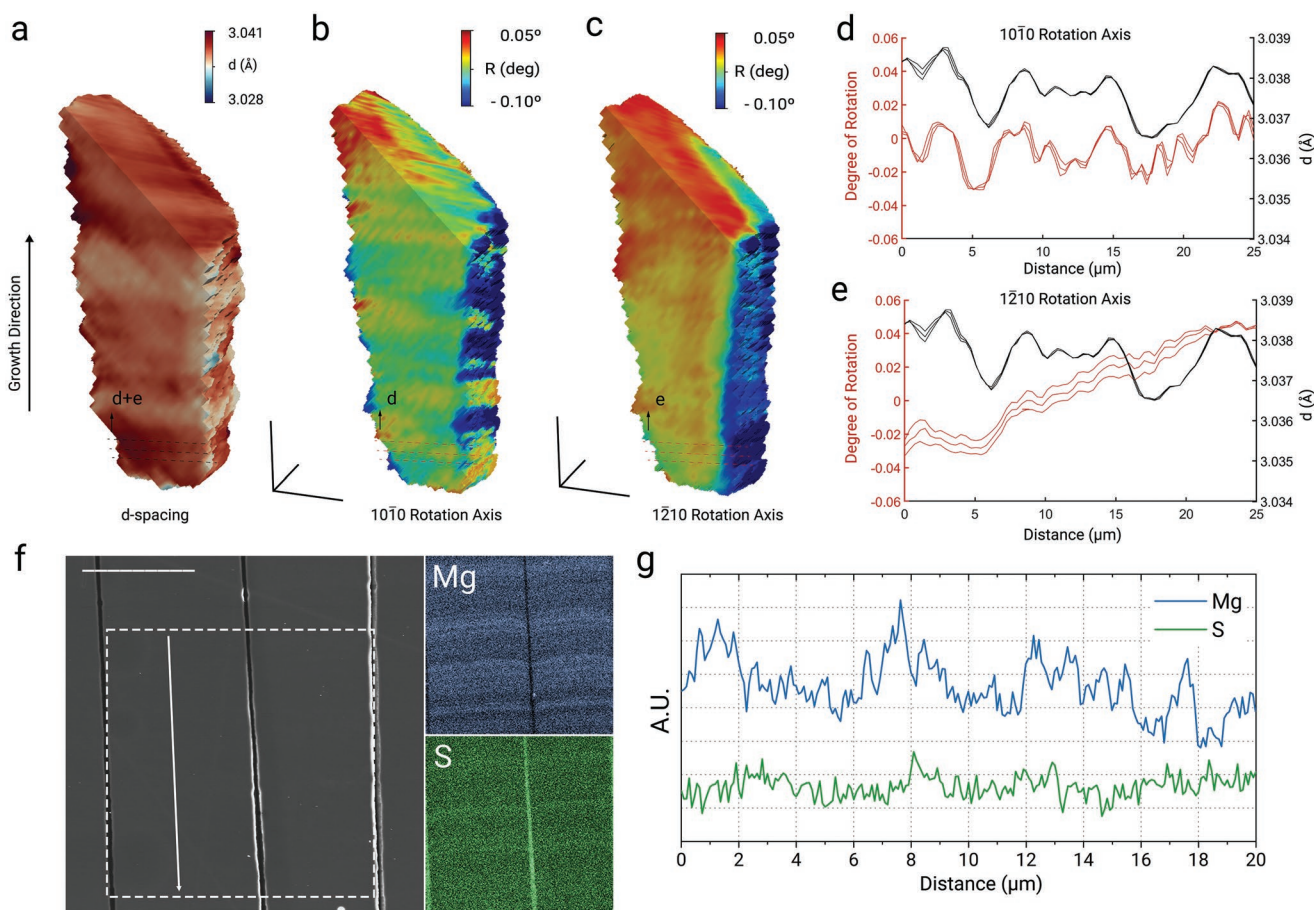


**Figure 4.** Correlative analysis of lattice orientation and spacing in a *P. nobilis* prism. a–c) Longitudinal sections of the first 25  $\mu\text{m}$  of a *P. nobilis* prism showing  $d$ -spacing, and lattice rotation around the  $[10\bar{1}0]$  axis and the  $[1\bar{2}10]$  axis, respectively. The isometric scalebars are 10  $\mu\text{m}$ . d,e) Lattice spacing along the direction of growth (black) calculated as the average value of all pixels on lines perpendicular to the direction of growth as indicated in (a), in comparison with rotations around the  $[10\bar{1}0]$  axis (d) and the  $[1\bar{2}10]$  axis (e). The plots show the lines average for three consecutive longitudinal slices. f) Energy-dispersive X-ray spectroscopy (EDS) maps of magnesium (Mg) and sulfur (S) content measured on a longitudinal section of the prisms in an area marked by a dashed line on an SEM image on the left. Scale bar: 10  $\mu\text{m}$ . g) Distribution of Mg and S along the long axis of the prisms (the direction of growth) measured along a line marked by an arrow in (f).

rotation around the  $[10\bar{1}0]$ -axis (Figure 4b) and around the  $[1\bar{2}10]$ -axis (Figure 4c). Astonishingly, when plotting lattice spacing against the measured lattice rotation along the long axis of the prism, a distinct correlation between lattice distortions and rotation around the  $[10\bar{1}0]$  axis (Figure 4d) is observed. The banding only slightly affects the rotation around the  $[1\bar{2}10]$  axis (Figure 4e). These data suggest that the registered rocking of the crystallographic orientation of calcite in the prisms, specifically the back and forth rotation around the  $\langle 10\bar{1}0 \rangle$  axis, is accompanied by local changes in lattice parameters of calcite.

Unidirectional growth of the prisms proceeds in a periodic rhythmic deposition of shell mineral leaving characteristic “growth lines” along the prisms—perpendicular to the direction of growth (Figure 1e).<sup>[28,40,46,47]</sup> As it is evident from energy-dispersive X-ray spectroscopy (EDS) maps taken from a longitudinal section of the prisms (Figure 4f), consecutive bands differ in the chemical composition of biogenic calcite, including relatively significant cyclic variation in the concentration of magnesium (Mg map) and slight changes in intracrystalline organic content represented by sulfur concentration (S map). The width of the observed bands (Figure 4g) correlates well with the periodicity of lattice distortions (Figure 4d) observed in this study.

Substitutional Mg ions and the incorporation of the organic phase in calcite was previously shown to have an effect on lattice parameters of calcite. The radius of Mg ions is smaller than that of Ca and therefore, substitution of  $\text{Ca}^{2+}$  by  $\text{Mg}^{2+}$  results in shrinkage of the calcitic lattice, as also demonstrated by the lattice parameters of dolomite with 50% of Mg cationic content. The effect of Mg replacement was previously predicted semi-empirically<sup>[13]</sup> and calculated in this work using modeling based on density functional theory (DFT) (Figure 5a–c). On the other hand, incorporation of the organic phase, depending on its location, is expected to increase the lattice parameters of the

mineral phase.<sup>[13,14,34]</sup> However, how do these phenomena cause synchronous alternation of the crystallographic orientation of calcite inside the prisms?

Previously reported lattice parameters of biogenic calcite in *P. nobilis* ( $a = 4.98138 \text{ \AA}$ ,  $c = 17.05803 \text{ \AA}$ , and  $d_{104} = 3.0328 \text{ \AA}$ ) at an average concentration of 1.71 at% Mg, measured here using inductively coupled plasma optical emission spectrometry (ICP-OES), suggest that the majority of organic molecules are located on the basal planes of calcite (Figure 5a–c). When comparing these data to numerical and semi-empirical predictions it is evident that while  $a$  lattice parameter of calcite is almost identical to the expected value after the correction of Mg ions substitution, the  $c$  parameter of calcite is increased. Similar observations were previously reported for a slightly larger concentration of Mg of 2 at%.<sup>[13]</sup> These anisotropic changes of lattice parameters result in an apparent periodic tilt of the oblique  $(10\bar{1}4)$  lattice planes, when in fact, the direction of the two axes remains unchanged.

Nevertheless, the DFXM data provides us with the opportunity to characterize the behavior of the lattice using the two chosen rotation axes:  $[10\bar{1}0]$  and  $[1\bar{2}10]$ . In fact, the selection of these specific directions allows us to deconvolute two types of lattice distortions. The direction normal to the  $(10\bar{1}4)$ -plane is  $[20\bar{2}1]$  (Figure 5d). In a hexagonal lattice, the angle between  $[20\bar{2}1]$  and  $[1\bar{2}10]$  is always  $90^\circ$  regardless of the lattice parameters of the material. Here, simply, the rotation axis lays in the  $(10\bar{1}4)$ -plane, which was used to produce the data and therefore, cannot generate information on lattice parameters. Hence, the rotation observed when analyzing this axis provides information on the real twist of the calcitic lattice in the prism. On the other hand, the angle between  $[20\bar{2}1]$  and  $[10\bar{1}0]$  depends on lattice parameters and, therefore, these data reflect anisotropic lattice distortions that can be falsely interpreted as a physical twist.

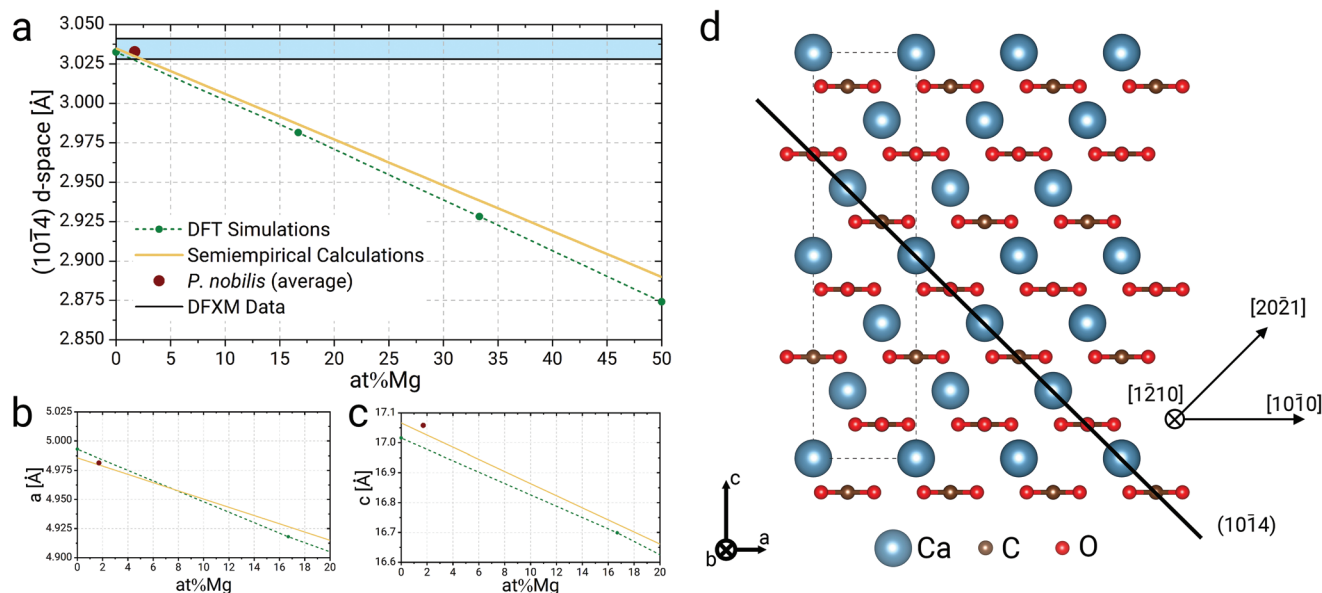


**Figure 5.** Analysis of lattice distortions in a *P. nobilis* prism. a–c)  $d_{104}$  spacing between the  $(10\bar{1}4)$  planes,  $a$  and  $c$  lattice parameter of biogenic calcite in *P. nobilis*, respectively, compared to semi-empirical<sup>[13]</sup> and DFT predictions as a function of Mg content. The  $d_{104}$  values as measured with DFXM are also shown. d) A ball and stick representation of the atomic structure of calcite showing the discussed crystallographic directions and planes.



### 3. Conclusions

The analysis of the two orthogonal data sets yields clear interpretation of the measured crystallographic properties of biogenic calcite in the prisms of *P. nobilis*. During growth, the organic molecules are incorporated on the basal plane of calcite. As a result, periodic changes in the concentration of Mg and the organic phase cause alternating anisotropic lattice distortions and inter-planar spacing. The entire calcific lattice, as described by the persistent bending of the *c*-axis (Figure 4e), gradually rotates around the  $[1\bar{2}10]$ -axis, which is perpendicular to one of the main slip direction of calcite  $r\{10\bar{1}4\}\langle\bar{2}021\rangle$  and is known to dominate at low temperatures during plastic deformation of non-biogenic calcite and has recently been shown to be present in biogenic calcite as well.<sup>[43,48]</sup> This outcome suggests that an additional force is exerted on the prism during its formation, causing a slight twist of the lattice. The force can be the result of a competitive growth of prisms that are spatially confined (Figure 1b),<sup>[8]</sup> asymmetry caused by inhomogeneous distribution of impurities or lattice misfit generated during calcite crystallization process.<sup>[43]</sup>

DFXM allowed us to put local crystallographic variations of biogenic calcite in a relatively large biomineral unit into perspective of the formation of the entire ultrastructure. DFXM measurements yielded 4D information on the evolution of morphological (macroscale) and local crystallographic (nanoscale) properties of the biomineral during growth with high spatial and angular resolution. Ultimately, careful analysis of the obtained data provided us with a unique opportunity to identify mechanisms that are responsible for the convoluted lattice behavior across scales and in 3D. It is important to note that the measurement of an additional diffraction spot could provide explicit knowledge on the local lattice parameters throughout the entire prism. We believe that this experimental approach will become key not only in the study of synthetic and geological materials systems but also in biological materials and biomineralization research.

### 4. Experimental Section

**Sample Preparation:** Shell pieces of *P. nobilis* were manually fractured parallel to the growth direction of the shell and coated with Pt/Pd for electron microscopy. Prisms were isolated for electron microscopy and DFXM. For this purpose, shell pieces of *P. nobilis* were immersed in a 4% sodium hypochlorite solution overnight at room temperature. The dispersed prisms were separated using a disposable filter system with a pore size of 40  $\mu\text{m}$ , extensively washed with Milli-Q water, and air dried. For EBSD investigations, pieces of the shell were embedded in poly(methyl methacrylate), cut parallel to the direction of growth, and polished with diamond and colloidal silica solutions. For ICP-OES measurements, to remove the organic membrane keeping the prisms together, segments of the prismatic structure were kept in 5% sodium hypochlorite solution for 15 min. The prisms separated from the bulk structure were then centrifuged and filtered.

**Electron Microscopy:** The fractured shell pieces and isolated prisms were coated with Pt/Pd samples and imaged using a Scios Dual Beam FIB/SEM (FEI/Thermo Fisher) in high-vacuum conditions.

**Electron Backscatter Diffraction Analysis (EBSD):** EBSD data were acquired with an EDAX Hikari Super EBSD system on a Scios Dual Beam FIB/SEM (FEI/Thermo Fisher). A low current of 1.6 nA and a voltage of 15 kV was used to minimize damage to the specimen surface by

the electron beam. The obtained EBSD patterns were processed using neighbor pattern averaging indexing.

**Energy-Dispersive X-ray Spectroscopy (EDS):** Elemental composition maps were obtained with a ZEISS Crossbeam 550 scanning electron microscope equipped with an Oxford X-Max 150 Silicon drift detectors. An accelerating voltage of 8 kV was used. To avoid charging, samples were carbon-coated.

**Dark-Field X-ray Microscopy (DFXM):** The DFXM measurements were performed at the beamline ID06-HXM at the European Synchrotron Radiation Facility (ESRF) in Grenoble, France. The beamline features a purpose-built experimental station (LAB Motion Systems, Leuven, Belgium) for DFXM. An energy of 17 keV was selected by a Si (111) double crystal monochromator and a Be translocator, located at 38.7 m from the x-ray source, pre-focused the X-rays onto another condenser consisting of a set of 58 vertically-focusing 1D Be lenses with an apex radius of 100  $\mu\text{m}$  (RXOptics, Juelich, Germany). The condenser creates a one-dimensionally focused line beam of 200 nm height at the sample position with adjustable width. For pre-characterization of the samples, a near-field camera, consisting of a FreLoN camera (ESRF, Atmel TH7899 CCD sensor chip, 2048  $\times$  2048 pixels, 16 bit) and optics designed and built by Optique Peter (Lentilly, France) to ESRF specifications,<sup>[22]</sup> was placed within millimeters of the samples and used to acquire bright-field radiographs of the prisms with an effective pixel size of 0.62  $\mu\text{m}^2$ . Diffraction images were recorded using a FreLoN camera (ESRF, Atmel TH7899 CCD sensor chip, 2048  $\times$  2048 pixels, 16 bit) bonded to a fiber optic taper with a scintillator (47.5  $\times$  47.5  $\mu\text{m}^2$  pixel size). The camera was mounted 188 mm behind the sample and diffraction patterns were recorded while rotating the samples to obtain complete diffraction patterns and to choose a suitable crystal plane and sample position for DFXM. Far-field dark-field images were obtained using an indirect detector mounted 5051 mm behind the sample on a frame allowing translations in the *xz* plane (AXMO, Brétigny-sur-Orge, France). The detector used a FreLoN camera (ESRF, Atmel TH7899 CCD sensor chip, 2048  $\times$  2048 pixels, 16 bit) with Olympus optics (UIS2 UPLANSapo 10 $\times$ /0.40 objective and U-TLU-1-2 tube lens) and a 10  $\mu\text{m}$  LuAG:Eu scintillator on a 170  $\mu\text{m}$  YAG substrate. This configuration produced a pixel size of 1.56  $\times$  1.56  $\mu\text{m}^2$  on the scintillator. The X-ray objective aligned in the diffracted beam used 88 Be lenslets with a 50  $\mu\text{m}$  apex radius (RXOptics, Juelich, Germany) with a working distance of 276 mm. Demagnification of the detector pixels by the objective produced a 78 nm pixel size at the sample; the projection along the beam axis degrades this resolution relative to the viewing angle ( $2\theta$ ). Real resolution was estimated to be  $\approx$ 100 nm due to optical imperfections in the Be lenses. Exposure time was 2 s per frame including readout. Full beam (400  $\mu\text{m}$   $\times$  400  $\mu\text{m}$ ) and condensed beam (400  $\mu\text{m}$   $\times$  200 nm) conditions were used. Eventually, as a consequence of vertical motion and step size, tilting increments and X-ray optics, a pixel size of 78, 315, and 1000 nm in *x*, *y*, and *z* directions, respectively, and an angular resolution of 0.01° were achieved.

**Inductively Coupled Plasma Optical Emission Spectrometry:** ICP-OES Optima 8000 from Perkin Elmer was employed to perform the experiments. For calibration, a multi-element standard from Carl Roth was used. 5 mg of prisms were mixed in 500  $\mu\text{L}$  of aqua regia (167  $\mu\text{L}$  HNO<sub>3</sub> + 333  $\mu\text{L}$  HCl). The mixture was then boiled for 2 h at 96 °C. After cooling, the solutions were diluted with water to 5 mL (10 $\times$  dilution).

**Density Functional Theory Modeling:** Calculations were run with the CRYSTAL17 package.<sup>[49]</sup> The PBE0-DC functional was used, containing 25% of exact Hartree–Fock exchange and an empirical long-range correction for oxygen–oxygen interactions, with coefficient fitted against the calcite versus aragonite enthalpy difference.<sup>[50]</sup> This method provides accurate structural parameters for carbonate phases while improving the description of their thermodynamic features with respect to that obtained with other DFT and DFT-D schemes. Basis sets and computational setup were the same as previously reported.<sup>[24]</sup> Calcite structures with 0%, 16.7%, 33.3%, and 50% Mg (dolomite) substitutions were modeled using calcite conventional cell as unit cell. Compositions with multiple options for site substitutions were all modeled to allow detecting the most stable and therefore more likely cationic distribution

(lowest energy). Optimized structures were used to predict the *d*-spacing of the (10 $\bar{1}$ 4) planes at different Mg compositions.

## Acknowledgements

The authors acknowledge the ESRF for the beam time at ID06-HXM. Financial support to I.Z. was provided by Bundesministerium für Bildung und Forschung through Grant 03Z22EN11. V.S. acknowledges support from STROBE: A National Science Foundation Science & Technology Center, under Grant No. DMR-1548924. R.D. acknowledges support from Curtin University, the Australian Research Council (DP160100677, FT180100385), and the Pawsey Supercomputing Centre and the Australian National Computational Infrastructure.

Open access funding enabled and organized by Projekt DEAL.

## Conflict of Interest

The authors declare no conflict of interest.

## Author Contributions

I.Z. conceived the study. I.Z., V.S., P.K.C., and C.D. performed the DFXM measurements. R.D. performed the DFT calculations. V.S. and P.K.C. analyzed the data. I.Z. and V.S. wrote the manuscript with the contribution from all authors.

## Data Availability Statement

The data that support the findings of this study are available from the corresponding author upon reasonable request.

## Keywords

biomineralization, calcite, crystal growth, dark-field X-ray microscopy, lattice disorder

Received: January 21, 2022

Revised: April 19, 2022

Published online: June 9, 2022

- [1] H. A. Lowenstam, S. Weiner, *On Biomineralization*, Oxford University Press, Oxford, UK **1989**.
- [2] P. Fratzl, R. Weinkamer, *Prog. Mater. Sci.* **2007**, *52*, 1263.
- [3] J. D. Taylor, M. Layman, *Palaeontology* **1972**, *15*, 73.
- [4] H. Gao, B. Ji, I. L. Jäger, E. Arzt, P. Fratzl, *Proc. Natl. Acad. Sci. USA* **2003**, *100*, 5597.
- [5] N. E. Waters, *Symp. Soc. Exp. Biol.* **1980**, *34*, 99.
- [6] S. Bellini, *Su di un particolare comportamento di batteri d'acqua dolce*, Institute of Microbiology, University of Pavia, Pavia, Italy **1963**.
- [7] A. Gal, V. Brumfeld, S. Weiner, L. Addadi, D. Oron, *Adv. Mater.* **2012**, *24*, OP77.
- [8] B. Bayerlein, P. Zaslansky, Y. Dauphin, A. Rack, P. Fratzl, I. Zlotnikov, *Nat. Mater.* **2014**, *13*, 1102.
- [9] I. Zlotnikov, V. Schoeppler, *Adv. Funct. Mater.* **2017**, *27*, 1700506.
- [10] V. Schoeppler, L. Gránásy, E. Reich, N. Poulsen, R. de Kloe, P. Cook, A. Rack, T. Pusztai, I. Zlotnikov, *Adv. Mater.* **2018**, *30*, 1803855.
- [11] M. Beliaev, D. Zöllner, A. Pacureanu, P. Zaslansky, I. Zlotnikov, *Nat. Phys.* **2021**, *17*, 410.
- [12] V. Schoeppler, R. Lemanis, E. Reich, T. Pusztai, L. Gránásy, I. Zlotnikov, *Proc. Natl. Acad. Sci. USA* **2019**, *116*, 20388.
- [13] B. Pokroy, A. N. Fitch, F. Marin, M. Kapon, N. Adir, E. Zolotoyabko, *J. Struct. Biol.* **2006**, *155*, 96.
- [14] B. Pokroy, A. Fitch, E. Zolotoyabko, *Adv. Mater.* **2006**, *18*, 2363.
- [15] F. Mastropietro, P. Godard, M. Burghammer, C. Chevallard, J. Daillant, J. Duboisset, M. Allain, P. Guenoun, J. Nouet, V. Chamard, *Nat. Mater.* **2017**, *16*, 946.
- [16] T. H. Metzger, Y. Politi, G. Carbone, B. Bayerlein, I. Zlotnikov, E. Zolotoyabko, P. Fratzl, *Cryst. Growth Des.* **2014**, *14*, 5275.
- [17] M. Cusack, *Palaeontology* **2016**, *59*, 171.
- [18] M. Beliaev, D. Zöllner, A. Pacureanu, P. Zaslansky, L. Bertineti, I. Zlotnikov, *J. Struct. Biol.* **2020**, *209*, 107432.
- [19] D. Baum, J. C. Weaver, I. Zlotnikov, D. Knötel, L. Tomholt, M. N. Dean, *Integr. Comp. Biol.* **2019**, *59*, 1700.
- [20] J. M. Walker, B. Marzec, N. Ozaki, D. Clare, F. Nudelman, *J. Struct. Biol.* **2020**, *210*, 107476.
- [21] H. Simons, A. C. Jakobsen, S. R. Ahl, C. Detlefs, H. F. Poulsen, *MRS Bull.* **2016**, *41*, 454.
- [22] M. Kutsal, P. Bernard, G. Berruyer, P. K. Cook, R. Hino, A. C. Jakobsen, W. Ludwig, J. Ormstrup, T. Roth, H. Simons, K. Smets, J. X. Sierra, J. Wade, P. Wattecamp, C. Yildirim, H. F. Poulsen, C. Detlefs, *IOP Conf. Ser. Mater. Sci. Eng.* **2019**, *580*, 012007.
- [23] I. Schmidt, E. Zolotoyabko, K. Lee, A. Gjardy, A. Berner, E. Lakin, P. Fratzl, W. Wagermaier, *Cryst. Res. Technol.* **2019**, *1–10*, 1900002.
- [24] J. Aufort, R. Demichelis, *Cryst. Growth Des.* **2020**, *20*, 8028.
- [25] F. Marin, G. Luquet, *Mater. Sci. Eng. C* **2005**, *25*, 105.
- [26] F. Nudelman, H. H. Chen, H. a. Goldberg, S. Weiner, L. Addadi, *Faraday Discuss.* **2007**, *136*, 9.
- [27] Y. Politi, J. Mahamid, H. Goldberg, S. Weiner, L. Addadi, *CrystEngComm* **2007**, *9*, 1171.
- [28] Y. Dauphin, J. Cuif, J. Doucet, M. Salomé, J. Susini, C. Williams, *Mar. Biol.* **2003**, *142*, 299.
- [29] J. P. Cuif, Y. Dauphin, G. Nehrke, J. Nouet, A. Perez-Huerta, *Minerals* **2012**, *2*, 11.
- [30] E. Seknazi, B. Pokroy, *Adv. Mater.* **2018**, *30*, 1707263.
- [31] C. A. Stiffler, J. E. Jakes, J. D. North, D. R. Green, J. C. Weaver, P. U. P. A. Gilbert, *Acta Biomater.* **2021**, *120*, 124.
- [32] I. Polishchuk, A. A. Bracha, L. Bloch, D. Levy, S. Kozachkevich, Y. Etinger-Geller, Y. Kauffmann, M. Burghammer, C. Giacobbe, J. Villanova, G. Hendler, C-Yu Sun, A. J. Giuffre, M. A. Marcus, L. Kundanati, P. Zaslansky, N. M. Pugno, P. U. P. A. Gilbert, A. Katsman, B. Pokroy, *Science* **2017**, *358*, 1294.
- [33] J.-B. Forien, C. Fleck, P. Cloetens, G. Duda, P. Fratzl, E. Zolotoyabko, P. Zaslansky, *Nano Lett.* **2015**, *15*, 3729.
- [34] E. Zolotoyabko, *Adv. Mater. Interfaces* **2017**, *4*, 1600189.
- [35] O. B. Bøggild, *K. Danks. Selsk. Skr. naturh. Math. Afd.* **1930**, *9*, 231.
- [36] J. G. Carter, G. R. Clark, *Notes a Short Course Stud. Geol.* **1985**, *13*, 50.
- [37] J.-P. Cuif, Y. Dauphin, G. Luquet, K. Medjoubi, A. Somogyi, A. Perez-Huerta, *Minerals* **2018**, *8*, 370.
- [38] A. G. Checa, J. T. Bonarski, M. G. Willinger, M. Faryna, K. Berent, B. Kania, A. González-Segura, C. M. Pina, J. Pospiech, A. Morawiec, *J. R. Soc. Interface* **2013**, *10*, 20130425.
- [39] I. C. Olson, R. A. Metzler, N. Tamura, M. Kunz, C. E. Killian, P. U. P. A. Gilbert, *J. Struct. Biol.* **2013**, *183*, 180.
- [40] Y. Dauphin, A. Brunelle, K. Medjoubi, A. Somogyi, J. Cuif, *Minerals* **2018**, *8*, 365.
- [41] F. Marin, N. Le Roy, B. Marie, *Front. Biosci.* **2012**, *S4*, 1099.
- [42] E. Reich, V. Schoeppler, R. Lemanis, E. Lakin, E. Zolotoyabko, D. Zöllner, I. Zlotnikov, *Acta Biomater.* **2019**, *85*, 272.
- [43] V. Schoeppler, D. Stier, R. J. Best, C. Song, J. Turner, B. H. Savitzky, C. Ophus, M. A. Marcus, S. Zhao, K. Bustillo, I. Zlotnikov, *Adv. Mater.* **2021**, *2101358*, 2101358.



- [44] D. Chateigner, M. Morales, E. M. Harper, *Mater. Sci. Forum* **2002**, 408–412, 1687.
- [45] F. Stöhr, J. Wright, H. Simons, J. Michael-Lindhard, J. Hübner, F. Jensen, O. Hansen, H. F. Poulsen, *J. Micromechanics Microengineering* **2015**, 25, 125013.
- [46] B. J. Meyerson, *Nature* **1968**, 217, 683.
- [47] J. Gordon, M. R. Carriker, *Science* **1978**, 202, 519.
- [48] J. H. P. De Bresser, C. J. Spiers, *Tectonophysics* **1997**, 272, 1.
- [49] R. Dovesi, F. Pascale, B. Civalleri, K. Doll, N. M. Harrison, I. Bush, P. D'Arco, Y. Noël, M. Rérat, P. Carbonnière, M. Causà, S. Salustro, V. Lacivita, B. Kirtman, A. M. Ferrari, F. S. Gentile, J. Baima, M. Ferrero, R. Demichelis, M. De La Pierre, *J. Chem. Phys.* **2020**, 152, 204111.
- [50] R. Demichelis, P. Raiteri, J. D. Gale, R. Dovesi, *J. Phys. Chem. C* **2013**, 117, 17814.